

Mechanisms Driving the Dispersal of Hydrothermal Iron From the Northern Mid Atlantic Ridge

Alessandro Tagliabue, Alastair Lough, Clément Vic, Vassil Roussenov, Jonathan Gula, Maeve Lohan, Joseph Resing, Richard Williams

▶ **To cite this version:**

Alessandro Tagliabue, Alastair Lough, Clément Vic, Vassil Roussenov, Jonathan Gula, et al.. Mechanisms Driving the Dispersal of Hydrothermal Iron From the Northern Mid Atlantic Ridge. Geophysical Research Letters, 2022, 49 (22), pp.e2022GL100615. 10.1029/2022GL100615 . hal-03926090

HAL Id: hal-03926090
https://cnrs.hal.science/hal-03926090

Submitted on 6 Jan 2023

HAL is a multi-disciplinary open access archive for the deposit and dissemination of scientific research documents, whether they are published or not. The documents may come from teaching and research institutions in France or abroad, or from public or private research centers.

L'archive ouverte pluridisciplinaire **HAL**, est destinée au dépôt et à la diffusion de documents scientifiques de niveau recherche, publiés ou non, émanant des établissements d'enseignement et de recherche français ou étrangers, des laboratoires publics ou privés.



Distributed under a Creative Commons Attribution 4.0 International License

Check for updates

19448007, ja, Downloaded from https://agupubs.onlinelibrary.wiley.com/doi/10.1029/2022GL100615 by University of California - Los Ange, Wiley Online Library on [09/11/2022]. See the Terms and Conditions (https://onlinelibrary.wiley.com/terms-and-conditions) on Wiley Online Library for rules of use; OA articles are governed by the applicable Creative Commons License

Accepted Article

Mechanisms driving the dispersal of hydrothermal iron from the northern Mid Atlantic Ridge

Alessandro Tagliabue[1], Alastair J. M. Lough[2,3], Clément Vic[4], Vassil Roussenov[1], Jonathan Gula[4,5], Maeve C. Lohan[2], Joseph A. Resing[6], Richard G. Williams[1]

[1]School of Environmental Sciences, University of Liverpool, UK
[2]School of Ocean and Earth Sciences, University of Southampton, UK
[3]University of Leeds, UK
[4]Univ Brest, CNRS, Ifremer, IRD, Laboratoire d'Océanographie Physique et Spatiale (LOPS), IUEM, 29280, Plouzané, France
[5]Institut Universitaire de France (IUF), Paris, France
[6]University of Washington, USA

Abstract The dispersal of dissolved iron (DFe) from hydrothermal vents is poorly constrained. Combining field observations and a modelling hierarchy, we find the dispersal of DFe from the Trans-Atlantic-Geotraverse vent site occurs predominantly in the colloidal phase and is controlled by multiple physical processes. Enhanced mixing near the seafloor and transport through fracture zones at fine-scales interacts with the wider ocean circulation to drive predominant westward DFe dispersal away from the Mid-Atlantic ridge at the 100km scale. In contrast, diapycnal mixing predominantly drives northward DFe transport within the ridge axial valley. The observed DFe dispersal is not reproduced by the coarse resolution ocean models typically used to assess ocean iron cycling due to their omission of local topography and mixing. Unless biogeochemical models account for fine-scale physics and colloidal Fe, they will inaccurately represent DFe dispersal from axial valley ridge systems, which make up half of the global ocean ridge crest.

Plain Language Summary

Hydrothermal venting along mid ocean ridges supplies large quantities of the trace metal iron to the ocean. Once it mixed with oxygenated seawater, precipitation leads to iron being lost from the dissolved phase to generate seafloor metal deposits. However, a small fraction of iron supplied escapes precipitation and remains in the dissolved phase. The processes that control the retention and ocean transport of hydrothermal dissolved iron is important as it has a disproportionate influence on the global carbon cycle. In this work we examined the processes driving the dispersal of dissolved iron from a major site of hydrothermal venting on the northern mid Atlantic ridge. We found that the complex topography of the mid Atlantic ridge was crucial in steering the escape of dissolved iron in the colloidal size range out of the immediate mid ocean ridge system. This raises challenges for the large scale ocean models used to represent the global ocean iron cycle as they are typically not parameterised at high enough spatial resolution. The use of multiple grids, with higher resolution nests, may offer a solution to the challenge of representing the interactions of tracer dispersal with complex topography.

Key points:

1. Iron is dispersed from TAG predominantly northward within the axial valley and westward off axis, dominated by the colloidal size fraction

This article has been accepted for publication and undergone full peer review but has not been through the copyediting, typesetting, pagination and proofreading process, which may lead to differences between this version and the Version of Record. Please cite this article as doi: 10.1029/2022GL100615.

This article is protected by copyright. All rights reserved.

2. A combination of fine-scale processes are necessary to explain the dispersal both within and outside the axial valley
3. Coarse resolution models are impaired in their ability to constrain the broader influence of iron supplied from axial valley ridge systems

1. Introduction

Dissolved iron (DFe) supply from hydrothermal vents has emerged as an important component of the ocean iron cycle [*Tagliabue et al.*, 2017]. Moreover, as hydrothermally sourced iron is ventilated in the iron-limited Southern Ocean, there is an important link to the ocean carbon cycle [*Resing et al.*, 2015; *Tagliabue et al.*, 2010; *Tagliabue and Resing*, 2016]. Consequently, there is a need to include hydrothermal DFe supply in ocean biogeochemical models to accurately represent the supply and cycling of this key micronutrient. Elevated iron signals have been observed in plumes above most mid ocean ridge systems [*Baker et al.*, 2002; *Gamo et al.*, 1996; *Hahm et al.*, 2015; *Massoth et al.*, 1994; *Rudnicki and Elderfield*, 1993]. More recently, as part of the GEOTRACES programme, iron has been shown to persist as DFe above and beyond the global ridge crest system [*Hatta et al.*, 2015; *Klunder et al.*, 2011; *Nishioka et al.*, 2013; *Resing et al.*, 2015; *Tagliabue et al.*, 2022]. Crucial in this growing role for hydrothermalism in shaping basin scale distributions is the question of how DFe is transported away from hydrothermal vent sites at the >100km scale [*Tagliabue and Resing*, 2016].

DFe (<0.2 μm) is an operational definition that encompasses a complex array of chemical species. In particular, contributions of biogenic and non-biogenic phases will play an important role in the colloidal size fraction (>0.02μm, but <0.2 μm) [*Tagliabue et al.*, 2017]. This is particularly true in hydrothermal settings, where large fluxes of reduced soluble forms of iron interact with oxygenated seawater to drive rapid changes in physico-chemical speciation [*Field and Sherrell*, 2000; *Rudnicki and Elderfield*, 1993]. In the deep ocean, colloidal and soluble forms of DFe have been observed to exist in a 1:1 ratio, but closer to iron sources or in the upper ocean the colloidal contribution can fluctuate notably [*Bergquist et al.*, 2007; *Fitzsimmons and Boyle*, 2014; *Kunde et al.*, 2019a; *Nishioka et al.*, 2001]. Colloidal iron is typically made up of iron (oxy)hydroxide phases and small lithogenic particles, as well as biomolecules and small bacteria or viruses that interact with organics [*Lough et al.*, 2019; *Tagliabue et al.*, 2017].

The global mid ocean ridge crest displays variable spreading rates and associated topographic settings, with potential implications for DFe supply and transport. Inert passive tracers of hydrothermal inputs, like mantle helium-3 (^{3}He), are elevated in basins with fast spreading ridges, like the Pacific, and depressed where ridge spreading rates are lower, like the Atlantic [*Jenkins et al.*, 2019]. This is important as although hydrothermal dFe inputs are parameterised in global models with constant DFe:^{3}He ratios following *Tagliabue et al.* [2010], hydrothermal DFe anomalies are higher than would be expected along the slow spreading mid Atlantic ridge based on ^{3}He values (e.g. [*Hatta et al.*, 2015; *Saito et al.*, 2013]). Adding further complexity is the fact that the slow spreading ridges like the mid-Atlantic ridge are typified by large axial valleys with topographic relief varying by kilometres across relatively small spatial scales. It is not known how resolving these scales of variability affects the

This article is protected by copyright. All rights reserved.

Accepted Article

19448007, ja, Downloaded from https://agupubs.onlinelibrary.wiley.com/doi/10.1029/2022GL100615 by University of California - Los Ange, Wiley Online Library on [09/11/2022]. See the Terms and Conditions (https://onlinelibrary.wiley.com/terms-and-conditions) on Wiley Online Library for rules of use; OA articles are governed by the applicable Creative Commons License

transport of DFe into the wider basin and the implications for coarse resolution ocean biogeochemical models that are typically used to test hypothesis about hydrothermal DFe supply and cycling [*Roshan et al.*, 2020; *Somes et al.*, 2021; *Tagliabue et al.*, 2022]. For instance, improved understanding of the critical processes and scales regulating the dispersal from ridges would aid our understanding of the necessary process resolution for ocean models. In that context, parameters such as topostrophy, which directly indicates the importance of topography to physical transports [*Holloway*, 2008], can be useful diagnostics.

Here we present new observations of DFe and colloidal Fe from the trans Atlantic geotraverse (TAG) hydrothermal site northern mid-Atlantic ridge as part of the UK GEOTRACES GA13 section. Our data document transport of DFe northwards within the axial valley and westward off axis into the wider basin at a range of spatial scales. Using a suite of model experiments at a range of resolutions, we diagnose the candidate physical processes that drive this behaviour and demonstrate that they are absent in coarse resolution models. This raises important questions about whether coarse resolution models are appropriate tools to explore iron cycle pathways associated with DFe supply from slow spreading ridge systems.

2. Methods

The UK GEOTRACES GA13 voyage sailed between Southampton and Guadeloupe in 2017/8 and as part of the sampling a detailed process study was conducted around the TAG hydrothermal vent system. A number of stations were sampled north and south of TAG within the axial valley, as well as east and west off axis into the Atlantic basin (Figure 1, Supplementary Figure 1). Station spacing ranged from 10-30km close to TAG and up to 100-200km for the farthest stations.

All sampling protocols followed those established by the GEOTRACES program [*Cutter et al.*, 2010]. Water samples were collected using Teflon coated Niskin-X bottles (Ocean Test Equipment) on a kevlar coated conducting wire. Water samples were filtered (0.2 µm, *Sartorius*) into acid clean low-density polyethylene bottles for DFe. A separate aliquot of seawater was filtered through 0.02 µm filters (Anotop, *Whatman*) for soluble Fe (SFe). All filtration was done in a class 100 clean laboratory on board the ship. Samples were acidified onboard to 0.024 M (UpA HCl, *Romil*). Samples were analysed for Fe concentrations using flow injection chemiluminescence [*Kunde et al.*, 2019b] and also via inductively coupled plasma mass spectrometry (*Thermoscientific, Element XR*) using a standard addition method. Measurements of GSP and GSC reference materials using flow injection and ICP-MS agree with consensus values (consensus: GSP 0.16 ± 0.05 nM, GSC 1.54 ± 0.12 nM and D2 0.94 ± 0.02 nM, with FIA measured GSP 0.15 ± 0.01 nM and GSC 1.52 ± 0.06, with ICP-MS measured GSC 1.48 ± 0.13 nM and D2 0.95 ± 0.06 nM).

Two Lagrangian dispersion experiments were carried out using the 3D velocity field of the GIGATL3 simulation. GIGATL3 is a regional simulation of the ocean physical state in the Atlantic Ocean based on the primitive-equation CROCO model, developed using the Regional Oceanic Modeling System [*Shchepetkin and McWilliams*, 2005]. The GIGATL3 simulation has a nominal horizontal resolution of 3 km and features 100 terrain-following vertical levels, with

This article is protected by copyright. All rights reserved.

Accepted Article

19448007, ja, Downloaded from https://agupubs.onlinelibrary.wiley.com/doi/10.1029/2022GL100615 by University of California - Los Ange, Wiley Online Library on [09/11/2022]. See the Terms and Conditions (https://onlinelibrary.wiley.com/terms-and-conditions) on Wiley Online Library for rules of use; OA articles are governed by the applicable Creative Commons License

stretching near the surface and seafloor (supplementary figure 2). The GIGATL3 bathymetry is taken from the global 30 arc second SRTM30plus data set [*Becker et al.*, 2009]. The initial state and lateral boundary conditions for velocity, sea surface height, temperature, and salinity are supplied by the Simple Ocean Data Assimilation data set [*Carton and Giese*, 2008]. Atmospheric forcing was supplied at hourly resolution by the Climate Forecast System Reanalysis [*Saha et al.*, 2010]. Tidal forcing derived from TPXO7 [*Egbert and Erofeeva*, 2002] is included. The 3D velocity field is saved hourly and linearly interpolated in space and time to perform two Lagrangian experiments using the Pyticles software [*Gula et al.*, 2014]. We used these two experiments to improve the robustness of the dispersion patterns and diagnostics are calculated using all particles across both experiments. The two experiments are strictly identical in terms of the particle seeding set up and integration time, only differing by starting point. The first experiment starts on 2008-08-29 whereas the second starts on 2010-06-05. Each experiment consists of releasing 25 particles every 6 h at the TAG vent site plume depth (as determined from helium data) for 8 months. The trajectories of the seeded particles are followed during the experiment. Diagnostics on particle spreading were performed for particles with ages between 10 and 180 days. As particles are continuously released, approximately 22000, 14000 or 5800 particles have an overall lifespan of 10, 90 or 180 days, respectively, for each experiment.

Modelling experiments are also conducted using a global scale ocean general circulation model. We conducted passive release experiments using two configurations of the Nucleus for European Modelling of the Ocean (NEMO) model. The first was the standard global configuration using the ORCA2 configuration at a horizontal resolution of 2 ^{o}x cos(latitude) curvilinear grid, with an enhancement to 0.5^{o} around the equator and 31 irregularly spaced vertical levels. This *NEMO-ORCA2* configuration is typical of those models coupled to biogeochemical models to address questions regarding biogeochemical cycling (e.g. *Tagliabue et al.,* 2022). We applied the default settings and boundary conditions of the reference configuration *ORCA2_ICE_PISCES* [*NEMO-Consortium*, 2019]. *NEMO-ORCA2* is forced with CORE-II normal year atmospheric forcing, with the NCAR bulk formulae [*Large and Yeager*, 2008]. After the initial spin-up, we conducted an idealised passive tracer release. The passive tracer concentration is continuously set to one at the deepest grid cell closest to the TAG site. The passive tracer fluxes at the surface, at the lateral boundaries and at the bottom are set to zero and the surface passive tracer concentration is restored to zero. The model is run for another 30 years (year 130 to 160) and the tracer spread is monitored. This scenario is repeated with a *NEMO-AGRIF* configuration with the addition of two nested regions, covering the TAG site, via adaptive mesh refinement package [*Debreu et al.*, 2008]. Two level, two-way nesting is used: the first level covers a region in the subtropical North Atlantic (dashed rectangle in supplementary figure 3) with refinement ratio of 4 in both latitude and longitude (to give a horizontal resolution of 1/2^{o}). The second level of nesting is applied over a region with the TAG site in the centre, with further refinement ratio of 4 (solid line rectangle in supplementary figure 3) reaching a horizontal resolution of 1/8^{o} or 12.48km. The passive tracer is released only in this high-resolution region. The model bathymetry of the two nested regions is constructed from the 5 arc minute resolution global bathymetry from ETOPO5. The initial conditions and the surface forcing functions of the nested regions in *NEMO-AGRIF* are interpolated from *NEMO-ORCA2* fields using the NEMO nesting tools.

This article is protected by copyright. All rights reserved.

Accepted Article

19448007, ja, Downloaded from https://agupubs.onlinelibrary.wiley.com/doi/10.1029/2022GL100615 by University of California - Los Ange, Wiley Online Library on [09/11/2022]. See the Terms and Conditions (https://onlinelibrary.wiley.com/terms-and-conditions) on Wiley Online Library for rules of use; OA articles are governed by the applicable Creative Commons License

Accepted Article

3. Results

3.1 Dispersion of DFe from the TAG hydrothermal vent field

The TAG site is a well-studied hydrothermal vent system, sited within the mid-Atlantic ridge axial valley (Figure 1). As part of the GA03 GEOTRACES section, DFe measurements were taken at TAG, but the station spacing for full-depth profiles exceeded 500km [*Hatta et al.*, 2015]. Within the axial valley DFe is predominantly dispersed northwards in the colloidal phase. The hydrothermal DFe anomaly of around 80 nM we observed at TAG matches that observed during the GA03 voyage [*Hatta et al.*, 2015] and persists at 3-4 nM at the stations 19 and 30km north (Figure 1). In contrast, DFe drops below concentrations of 2 nM for the station 30km south, indicating greater dilution and/or removal from the dissolved phase (Figure 1). At TAG, the highest concentrations of DFe are associated with very low soluble Fe fraction (<10%), indicating the dominance of colloidal Fe. At the depths of the greatest hydrothermal DFe signals, the soluble Fe fraction within the axial valley also remains low (<25%) within 30km of TAG, again indicating dominance of Fe colloids in the hydrothermal DFe signal throughout the valley.

There is a contrasting DFe signal east and west from TAG off axis from the mid-Atlantic ridge. At the largest spatial scales, strong hydrothermal DFe anomalies persist 140-250km west of TAG (stations 28 and 29), but are absent at stations 140-250km to the east (stations 33 and 32). A marked dFe anomaly between 2,200-3,400m (centered on 3000m) of 2.64nM 140km from TAG (station 29) declines to a more localised anomaly of 0.95nM 250km west of TAG (station 28). Both of these DFe signals are above the concentrations observed at this depth and latitude at the eastern stations. Notably, the elevated DFe concentrations 140-250km west of TAG remain associated with low soluble DFe fractions, indicating the importance of Fe colloids. Consistent with the absence of hydrothermal DFe input or transport, the soluble iron fraction 140-250km to the east is closer to the 50% typically observed in the deep ocean [*Kunde et al.*, 2019a].

3.2 Processes shaping the dispersion from TAG over different space and time scales

The particle release experiments conducted with the high-resolution particle tracking model reveal the role of different processes shaping dispersion from TAG over different space and timescales (Figure 2). We particularly note three stages of physical dispersal.

10-30 days: In the immediate period following their release, particles preferentially spread within the axial valley in a northeast-southwest direction, largely under topographic control (Figure 2ab). The impact of topography is illustrated by the topostrophy parameter, τ [*Holloway*, 2008], which is elevated and positive within the valley and much reduced off axis (Supplementary Figure 4). That τ is >0 indicates a cyclonic circulation within the axial valley basins, consistent with observed and modelled circulations within the MAR valley [*Lahaye et al.*, 2019]. The topography of the mid Atlantic ridge axial valley also allows particles to rapidly escape the axial

This article is protected by copyright. All rights reserved.

19448007, ja, Downloaded from https://agupubs.onlinelibrary.wiley.com/doi/10.1029/2022GL100615 by University of California - Los Ange, Wiley Online Library on [09/11/2022]. See the Terms and Conditions (https://onlinelibrary.wiley.com/terms-and-conditions) on Wiley Online Library for rules of use; OA articles are governed by the applicable Creative Commons License

valley along isopycnal surfaces to the southwest via fracture zones within only a few days (Figure 2a).

60-90 days: Particles that escape the valley spread isotropically along density surfaces (Figures 2c,d). The topographic control is now very weak on average as topographic slopes are weaker and particles are now well above the seafloor (Supplementary Figure 4). Consequently, particles spread mostly along isopycnals due to the lesser influence of diapycnal mixing processes that were occurring on and within the axial valley system.

120-180 days: After 4-6 months, particles preferentially spread westward outside the axial valley (Figure 2ef) due to the combination of the large-scale mean sub-tropical gyre circulation and the planetary beta effect that constrains mesoscale vortices to travel westward [*Killworth*, 1983; *Nof*, 1981]. By this stage, transport within the axial valley also demonstrates a predominantly northward signal as particles fill the northern axial valley basin within the mid-Atlantic ridge north of TAG. Notably, dispersal westward off axis into the wider Atlantic Ocean basin and northward within the axial valley matches the observed DFe concentration anomalies closely (Figures 1 and 3e), as well as understanding from prior work [*Thurnherr et al.*, 2002; *Vic et al.*, 2018; *Yearsley et al.*, 2020].

3.3 The importance of bottom topography in representing hydrothermal Fe supply in global ocean models

The set of simulations conducted with two NEMO allow us to explore how the dispersion of hydrothermal tracers from TAG are represented by coarse resolution *NEMO-ORCA2* global models and with the *NEMO-AGRIF* configuration. The *NEMO-AGRIF* configuration has a 1/8^{o} (or 12.48km) resolution regional nested grid around TAG (supplementary figure 3), but the vertical resolution of *NEMO-AGRIF* and *NEMO-ORCA2* are around three-fold lower than the particle tracking model. This set of model configurations were designed to link the very high-resolution regional modelling with the types of models used for larger scale biogeochemical modelling that tend to have horizontal resolutions of between 1-5^{o} [*Roshan et al.*, 2020; *Somes et al.*, 2021; *Tagliabue et al.*, 2022].

In general, the *NEMO-AGRIF* model shows very similar dispersal patterns to the high-resolution particle model, with strong signals remaining localised within the axial valley and spreading preferentially north within the axial valley and westward off-axis (Figure 3). In contrast, the *NEMO-ORCA2* configuration typically used for assessments of iron biogeochemistry show two major deficiencies, relative to the nested *NEMO-AGRIF* and high-resolution particle models (Figure 2), as well as the observations (Figure 1). First, high concentrations of tracer do not remain trapped in the ridge system (Figure 3a). Second, large scale dispersal operates equally away from the ridge both east and west, rather than predominantly to the west (Figure 3a, c). These deficiencies in the zonal dispersal can be illustrated by a section taken along 26^{o}N, with the *NEMO-AGRIF* nested model displaying dispersal was (i) more restricted and (ii) predominantly westward as compared to the coarse resolution *NEMO-ORCA2* model. Notably, both *NEMO-ORCA2* and *NEMO-AGRIF* share the same number and arrangement of vertical levels, highlighting the importance of the horizontal resolution in improving the agreement with both high-resolution particle

This article is protected by copyright. All rights reserved.

Accepted Article

19448007, ja, Downloaded from https://agupubs.onlinelibrary.wiley.com/doi/10.1029/2022GL100615 by University of California - Los Ange, Wiley Online Library on [09/11/2022]. See the Terms and Conditions (https://onlinelibrary.wiley.com/terms-and-conditions) on Wiley Online Library for rules of use; OA articles are governed by the applicable Creative Commons License

tracking models and inferences regarding dispersal gleaned from direct observations of DFe. To compare the model configurations more directly against observations we merged the GA13 data from this study with DFe observations from the GA03 GEOTRACES section that followed the same cruise track, which displays a similar westward propagation off axis from TAG (Figure 3e).

4. Discussion

4.1 Processes driving the dispersal of iron from the mid-Atlantic ridge

Dispersal of DFe from TAG is controlled by a combination of local mixing across density surfaces and the specific geometry of the mid Atlantic ridge. Using our particle tracking simulations, we tracked the cumulative changes in density during the particle lifetimes to identify the importance of across isopycnal mixing in explaining whether DFe dispersal west of TAG (Figure 3e) is over or around topography. Enhanced mixing is associated with small scale internal tides and mesoscale currents interacting with topographic features, such as mid ocean ridges [*Vic et al.*, 2019]. The average cumulative change in density across all particles highlights strong transfer to lighter density surfaces on the ridge crest and within the axial valley (Figure 4a). Small average changes outside the axial valley are associated with large variability (Figure 4b). Focussing on an example site outside the valley, we can see that while average cumulative density changes are close to zero, 64% of all particles experience lightening (Figure 4c, Supplementary Figure 5), leading to around 200m elevation in absolute depth (Figure 4d). Within the valley, the change in cumulative density is much more striking (Figure 4c), with changes in absolute elevation of closer to 100m (Figure 4d). The larger changes in absolute depth, despite smaller changes in cumulative density outside the valley are associated with slumping and heaving of isopycnal layers. Overall, the significant population of particles outside the valley without strong cumulative density changes demonstrates the transfer of particles through fracture zones and highlights the role of local geometry of the mid Atlantic ridge system (see Sec 3.2 and 3.3, Supplementary Figure 5). Within the valley, across density mixing associated with topography is much more important.

By examining the lifetime of particles reaching the local particle maxima at any given location, we can quantify timescales of dispersion across the two Lagrangian experiments (Figure 4e). Dispersion from TAG takes at least 100 days to reach 140km west of TAG (station 29) or exceeds 150 days to reach station 28 at 250km from TAG (Figure 4). Since most hydrothermal iron is associated with maxima in colloidal Fe, this indicates relatively strong stability of colloidal iron phases during transport (for at least 6 months). We note that these estimates should be seen as minimum estimates for transport to the different locations. If we integrated the particle model longer, we would potentially also observe the arrival of older particles and find evidence for longer term stability of colloidal iron. The extended lifetime of colloidal iron may be driven by slower oxidation of colloidal iron [*Gartman and Luther*, 2014] or its association with organic phases [*Fitzsimmons et al.*, 2017]. In previous work, the 'log scale distance' (i.e. estimation of the tracer decay from a source) has been used to estimate the loss of DFe during water mass movement, typically with a two phases of rapid and slow removal close to sources [*Jensen et al.*, 2020]. We find a log scale distance of around 56km for DFe from TAG using stations

This article is protected by copyright. All rights reserved.

Accepted Article

19448007, ja, Downloaded from https://agupubs.onlinelibrary.wiley.com/doi/10.1029/2022GL100615 by University of California - Los Ange, Wiley Online Library on [09/11/2022]. See the Terms and Conditions (https://onlinelibrary.wiley.com/terms-and-conditions) on Wiley Online Library for rules of use; OA articles are governed by the applicable Creative Commons License

35, 28 and 29 (spanning 0, 140 and 240km from source, Figure 1), similar to values seen in coastal waters [*Jensen et al.*, 2020; *Wong et al.*, 2022]. This estimate is likely skewed by the high concentration TAG end member of >75nM, and more observations at the 100-1000km scale would help refine estimates for longer range transport from TAG at concentrations <2 nM.

4.2 Using model-observation studies to quantify iron cycle mechanisms

Combining global ocean biogeochemical modelling experiments with GEOTRACES datasets have played a key role in identifying significant processes shaping the ocean iron cycle and their wider impacts. However, their results may be compromised when the model resolution is insufficient for the system of interest. Our results show that only model experiments at the 10s of km horizontal resolution can accurately represent the dispersal of DFe from the TAG site on the mid-Atlantic ridge, far exceeding the typical resolution of global ocean biogeochemical models (100-500km). This is due to the complex topography of the axial valley setting of the TAG site that is not resolved in global ocean biogeochemical models. Where ridge topography is less variable, for instance at faster ridge spreading sites with shallower axial valleys or troughs, e.g. the East Pacific Rise, coarser resolutions may be sufficient [*Resing et al.*, 2015]. Our results suggest that new solutions, accounting for high-resolution sub grids, are required to properly represent DFe dispersal at scales exceeding 100km from the axial valley settings that make up around half of the mid ocean ridge crest. Improved vertical resolution may also be important, but this was not assessed directly in this study as both NEMO model configurations had the same number and arrangement of vertical levels. For the transport of Fe specifically, our observations highlight that explicitly accounting for the speciation of DFe, especially colloidal phases, is a critical component.

The role of representing DFe input and wider transport around local topography in coarse resolution models may be more generically relevant. For instance, continental shelves can also be associated with complex topographic geometry and coarse resolution models may face similar challenges in properly representing the dispersal of tracers supplied, such as DFe. For instance, in the North Pacific, the DFe inputs from sediment resuspension disperses from the sea of Okhotsk into the wider North Pacific basin via North Pacific Intermediate Water (NPIW) [*Nishioka et al.*, 2021; *Nishioka et al.*, 2020]. An important component of this dispersal is the strong topographically induced diapycnal mixing that occurs over the Kuril straits [*Yagi and Yasuda*, 2012], transporting DFe onto the NPIW isopycnals to then spread throughout the North Pacific basin [*Nishioka et al.*, 2020]. Tidal mixing along the shelf break may also be an important component of DFe supply in the southern Bering Sea [*Tanaka et al.*, 2012], as well as seamounts [*Lavelle et al.*, 2004]. Therefore, it is important to consider any biases in the DFe dispersal from both hydrothermal and sediment inputs that may arise from insufficient resolution in process-based models.

5. Conclusions

Using a novel sampling strategy at a scale of 10s and 100s of km around the TAG vent site, we document the predominant transport pathways of hydrothermal DFe. Our observations indicated DFe was transported northward within the axial valley

This article is protected by copyright. All rights reserved.

Accepted Article

19448007, ja, Downloaded from https://agupubs.onlinelibrary.wiley.com/doi/10.1029/2022GL100615 by University of California - Los Ange, Wiley Online Library on [09/11/2022]. See the Terms and Conditions (https://onlinelibrary.wiley.com/terms-and-conditions) on Wiley Online Library for rules of use; OA articles are governed by the applicable Creative Commons License

and westward off axis in the colloidal size fraction. Dispersal within the valley arose due to the diapycnal mixing that resulted from topographic interaction. Transport off axis resulted from both diapycnal mixing and the fine scales of axial valley geometry, especially fracture zones. The dispersal patterns of DFe were reproduced with a high-resolution particle tracking model and a global model with a nested ~10km horizontal grid, but not with a global ocean configuration. This raises challenges for correctly representing DFe supply and the associated biogeochemical impacts from axial valley hydrothermal vent systems, as well as other supply mechanisms around local topographical features. The accurate representation of dispersal from such systems will require sufficient model resolution to be capable of representing the internal Rossby radius of deformation (which itself depends on latitude and stratification), as well as to resolve abyssal hills and troughs around mid-ocean ridge systems. Further work is needed to develop sufficiently efficient solutions to represent these processes in global models that resolve multiple biogeochemical tracers and assess the implications of their neglect more broadly.

6. Acknowledgements

This work is part of the United Kingdom GEOTRACES section GA13 which was supported by the Natural Environment Research Council (NERC) Grants NE/N009525/1 to AT and NE/N010396/1 to MCL. We thank the Captain and crew of the *RRS James Cook* and everyone that contributed to the GA13 sampling effort on board. JG acknowledges support from the French National Agency for Research (ANR) through the project DEEPER (ANR-19- CE01-0002-01), and PRACE and GENCI for awarding access to HPC resources Joliot-Curie Rome and SKL from GENCI-TGCC (grants 2020-A0090112051, 2019gch0401, and PRACE project 2018194735) and HPC facilities DATARMOR of “Pôle de Calcul Intensif pour la Mer” at Ifremer Brest France. The authors thank Gildas Cambon and Sébastien Theetten for their contribution in the development of the GIGATL3 simulation. JAR was funded by NOAA Ocean Exploration and Earth Ocean Interactions program; this is PMEL #XXX and CICOES publication # YYYY. The International GEOTRACES Programme is possible in part thanks to the support from the U.S. National Science Foundation (Grant OCE-1840868) to the Scientific Committee on Oceanic Research (SCOR). We thank the two reviewers for their comments that improved the final submission.

Data availability statement:

CROCO ocean model is available at https://www.croco-ocean.org. Information about the GIGATL6 simulation can be found at https://doi. org/10.5281/zenodo.4948523

The Lagrangian software Pyticles is available at https://github.com/Mesharou/Pyticles and has been archived on Zenodo at https://doi.org/10.5281/zenodo.4973786.

The data from the GA13 transect is available (to view and download) as part of the GEOTRACES intermediate data product 2021 which can be accessed online via https://www.geotraces.org/geotraces-intermediate-data-product-2021/

7. References

This article is protected by copyright. All rights reserved.

Accepted Article

19448007, ja, Downloaded from https://agupubs.onlinelibrary.wiley.com/doi/10.1029/2022GL100615 by University of California - Los Ange, Wiley Online Library on [09/11/2022]. See the Terms and Conditions (https://onlinelibrary.wiley.com/terms-and-conditions) on Wiley Online Library for rules of use; OA articles are governed by the applicable Creative Commons License

Accepted Article

Baker, E. T., et al. (2002), Hydrothermal venting along Earth's fastest spreading center: East Pacific Rise, 27.5°-32.3°, *Journal of Geophysical Research: Solid Earth*, *107*(B7), EPM 2-1-EPM 2-14, doi:10.1029/2001jb000651.

Becker, J. J., et al. (2009), Global Bathymetry and Elevation Data at 30 Arc Seconds Resolution: SRTM30_PLUS, *Marine Geodesy*, *32*(4), 355-371, doi:10.1080/01490410903297766.

Bergquist, B. A., J. Wu, and E. A. Boyle (2007), Variability in oceanic dissolved iron is dominated by the colloidal fraction, *Geochimica et Cosmochimica Acta*, *71*(12), 2960-2974, doi:10.1016/j.gca.2007.03.013.

Carton, J. A., and B. S. Giese (2008), A Reanalysis of Ocean Climate Using Simple Ocean Data Assimilation (SODA), *Monthly Weather Review*, *136*(8), 2999-3017, doi:10.1175/2007mwr1978.1.

Cutter, G., P. Andersson, L. Codispoti, P. Croot, R. François, M. C. Lohan, H. Obata, and M. Rutgers v. d. Loeff (2010), Sampling and Sample-handling Protocols for GEOTRACES Cruises, edited, doi:https://epic.awi.de/id/eprint/34484.

Debreu, L., C. Vouland, and E. Blayo (2008), AGRIF: Adaptive grid refinement in Fortran, *Computers & Geosciences*, *34*(1), 8-13, doi:10.1016/j.cageo.2007.01.009.

Egbert, G. D., and S. Y. Erofeeva (2002), Efficient Inverse Modeling of Barotropic Ocean Tides, *Journal of Atmospheric and Oceanic Technology*, *19*(2), 183-204, doi:10.1175/1520-0426(2002)019<0183:Eimobo>2.0.Co;2.

Field, M. P., and R. M. Sherrell (2000), Dissolved and particulate Fe in a hydrothermal plume at 9°45′N, East Pacific Rise, *Geochimica et Cosmochimica Acta*, *64*(4), 619-628, doi:10.1016/s0016-7037(99)00333-6.

Fitzsimmons, J. N., and E. A. Boyle (2014), Both soluble and colloidal iron phases control dissolved iron variability in the tropical North Atlantic Ocean, *Geochimica et Cosmochimica Acta*, *125*, 539-550, doi:10.1016/j.gca.2013.10.032.

Fitzsimmons, J. N., S. G. John, C. M. Marsay, C. L. Hoffman, Sarah L. Nicholas, B. M. Toner, C. R. German, and R. M. Sherrell (2017), Iron persistence in a distal hydrothermal plume supported by dissolved–particulate exchange, *Nature Geoscience*, *10*(3), 195-201, doi:10.1038/ngeo2900.

Gamo, T., et al. (1996), Hydrothermal plumes at the Rodriguez triple junction, Indian ridge, *Earth and Planetary Science Letters*, *142*(1-2), 261-270, doi:10.1016/0012-821x(96)00087-8.

Gartman, A., and G. W. Luther (2014), Oxidation of synthesized sub-micron pyrite (FeS2) in seawater, *Geochimica et Cosmochimica Acta*, *144*, 96-108, doi:10.1016/j.gca.2014.08.022.

Gula, J., M. J. Molemaker, and J. C. McWilliams (2014), Submesoscale cold filaments in the Gulf Stream, *Journal of Physical Oceanography*, *44*(10), 2617-2643, doi:10.1175/JPO-D-14-0029.1s.

This article is protected by copyright. All rights reserved.

19448007, ja, Downloaded from https://agupubs.onlinelibrary.wiley.com/doi/10.1029/2022GL100615 by University of California - Los Ange, Wiley Online Library on [09/11/2022]. See the Terms and Conditions (https://onlinelibrary.wiley.com/terms-and-conditions) on Wiley Online Library for rules of use; OA articles are governed by the applicable Creative Commons License

Hahm, D., E. T. Baker, T. Siek Rhee, Y.-J. Won, J. A. Resing, J. E. Lupton, W.-K. Lee, M. Kim, and S.-H. Park (2015), First hydrothermal discoveries on the Australian-Antarctic Ridge: Discharge sites, plume chemistry, and vent organisms, *Geochemistry, Geophysics, Geosystems*, *16*(9), 3061-3075, doi:10.1002/2015gc005926.

Hatta, M., C. I. Measures, J. Wu, S. Roshan, J. N. Fitzsimmons, P. Sedwick, and P. Morton (2015), An overview of dissolved Fe and Mn distributions during the 2010–2011 U.S. GEOTRACES north Atlantic cruises: GEOTRACES GA03, *Deep Sea Research Part II: Topical Studies in Oceanography*, *116*, 117-129, doi:10.1016/j.dsr2.2014.07.005.

Holloway, G. (2008), Observing global ocean topostrophy, *Journal of Geophysical Research*, *113*(C7), doi:10.1029/2007jc004635.

Jenkins, W. J., et al. (2019), A comprehensive global oceanic dataset of helium isotope and tritium measurements, *Earth System Science Data*, *11*(2), 441-454, doi:10.5194/essd-11-441-2019.

Jensen, L. T., et al. (2020), A comparison of marine Fe and Mn cycling: U.S. GEOTRACES GN01 Western Arctic case study, *Geochimica et Cosmochimica Acta*, *288*, 138-160, doi:10.1016/j.gca.2020.08.006.

Killworth, P. D. (1983), On the Motion of Isolated Lenses on a Beta-Plane, *Journal of Physical Oceanography*, *13*(3), 368-376, doi:10.1175/1520-0485(1983)013<0368:Otmoil>2.0.Co;2.

Klunder, M. B., P. Laan, R. Middag, H. J. W. De Baar, and J. C. van Ooijen (2011), Dissolved iron in the Southern Ocean (Atlantic sector), *Deep Sea Research Part II: Topical Studies in Oceanography*, *58*(25-26), 2678-2694, doi:10.1016/j.dsr2.2010.10.042.

Kunde, K., N. J. Wyatt, D. González-Santana, A. Tagliabue, C. Mahaffey, and M. C. Lohan (2019a), Iron Distribution in the Subtropical North Atlantic: The Pivotal Role of Colloidal Iron, *Global Biogeochemical Cycles*, *33*(12), 1532-1547, doi:10.1029/2019gb006326.

Kunde, K., N. J. Wyatt, D. González-Santana, A. Tagliabue, C. Mahaffey, and M. C. Lohan (2019b), Iron Distribution in the Subtropical North Atlantic: The Pivotal Role of Colloidal Iron, *Global Biogeochemical Cycles*, doi:10.1029/2019gb006326.

Lahaye, N., J. Gula, A. M. Thurnherr, G. Reverdin, P. Bouruet-Aubertot, and G. Roullet (2019), Deep Currents in the Rift Valley of the North Mid-Atlantic Ridge, *Frontiers in Marine Science*, *6*, doi:10.3389/fmars.2019.00597.

Large, W. G., and S. G. Yeager (2008), The global climatology of an interannually varying air–sea flux data set, *Climate Dynamics*, *33*(2-3), 341-364, doi:10.1007/s00382-008-0441-3.

This article is protected by copyright. All rights reserved.

Accepted Article

19448007, ja, Downloaded from https://agupubs.onlinelibrary.wiley.com/doi/10.1029/2022GL100615 by University of California - Los Ange, Wiley Online Library on [09/11/2022]. See the Terms and Conditions (https://onlinelibrary.wiley.com/terms-and-conditions) on Wiley Online Library for rules of use; OA articles are governed by the applicable Creative Commons License

Lavelle, J. W., I. D. Lozovatsky, and D. C. Smith (2004), Tidally induced turbulent mixing at Irving Seamount-Modeling and measurements, *Geophysical Research Letters*, *31*(10), n/a-n/a, doi:10.1029/2004gl019706.

Lough, A. J. M., W. B. Homoky, D. P. Connelly, S. A. Comer-Warner, K. Nakamura, M. K. Abyaneh, B. Kaulich, and R. A. Mills (2019), Soluble iron conservation and colloidal iron dynamics in a hydrothermal plume, *Chemical Geology*, *511*, 225-237, doi:10.1016/j.chemgeo.2019.01.001.

Massoth, G. J., E. T. Baker, J. E. Lupton, R. A. Feely, D. A. Butterfield, K. L. Von Damm, K. K. Roe, and G. T. Lebon (1994), Temporal and spatial variability of hydrothermal manganese and iron at Cleft segment, Juan de Fuca Ridge, *Journal of Geophysical Research: Solid Earth*, *99*(B3), 4905-4923, doi:10.1029/93jb02799.

NEMO-Consortium (2019), NEMO Reference configurations inputs (v4.0.1), doi:10.5281/zenodo.1471701.

Nishioka, J., H. Obata, T. Hirawake, Y. Kondo, Y. Yamashita, K. Misumi, and I. Yasuda (2021), A review: iron and nutrient supply in the subarctic Pacific and its impact on phytoplankton production, *Journal of Oceanography*, *77*(4), 561-587, doi:10.1007/s10872-021-00606-5.

Nishioka, J., H. Obata, H. Ogawa, K. Ono, Y. Yamashita, K. Lee, S. Takeda, and I. Yasuda (2020), Subpolar marginal seas fuel the North Pacific through the intermediate water at the termination of the global ocean circulation, *Proceedings of the National Academy of Sciences*, *117*(23), 12665-12673, doi:doi:10.1073/pnas.2000658117.

Nishioka, J., H. Obata, and D. Tsumune (2013), Evidence of an extensive spread of hydrothermal dissolved iron in the Indian Ocean, *Earth and Planetary Science Letters*, *361*, 26-33, doi:10.1016/j.epsl.2012.11.040.

Nishioka, J., S. Takeda, C. S. Wong, and W. K. Johnson (2001), Size-fractionated iron concentrations in the northeast Pacific Ocean: distribution of soluble and small colloidal iron, *Marine Chemistry*, *74*(2-3), 157-179, doi:10.1016/s0304-4203(01)00013-5.

Nof, D. (1981), On the β-Induced Movement of Isolated Baroclinic Eddies, *Journal of Physical Oceanography*, *11*(12), 1662-1672, doi:10.1175/1520-0485(1981)011<1662:Otimoi>2.0.Co;2.

Resing, J. A., P. N. Sedwick, C. R. German, W. J. Jenkins, J. W. Moffett, B. M. Sohst, and A. Tagliabue (2015), Basin-scale transport of hydrothermal dissolved metals across the South Pacific Ocean, *Nature*, *523*(7559), 200-203, doi:10.1038/nature14577.

Roshan, S., T. DeVries, J. Wu, S. John, and T. Weber (2020), Reversible scavenging traps hydrothermal iron in the deep ocean, *Earth and Planetary Science Letters*, *542*, doi:10.1016/j.epsl.2020.116297.

Rudnicki, M. D., and H. Elderfield (1993), A chemical model of the buoyant and neutrally buoyant plume above the TAG vent field, 26 degrees N, Mid-Atlantic Ridge,

This article is protected by copyright. All rights reserved.

Accepted Article

19448007, ja, Downloaded from https://agupubs.onlinelibrary.wiley.com/doi/10.1029/2022GL100615 by University of California - Los Ange, Wiley Online Library on [09/11/2022]. See the Terms and Conditions (https://onlinelibrary.wiley.com/terms-and-conditions) on Wiley Online Library for rules of use; OA articles are governed by the applicable Creative Commons License

Geochimica et Cosmochimica Acta, *57*(13), 2939-2957, doi:10.1016/0016-7037(93)90285-5.

Saha, S., et al. (2010), The NCEP Climate Forecast System Reanalysis, *Bulletin of the American Meteorological Society*, *91*(8), 1015-1058, doi:10.1175/2010bams3001.1.

Saito, M. A., A. E. Noble, A. Tagliabue, T. J. Goepfert, C. H. Lamborg, and W. J. Jenkins (2013), Slow-spreading submarine ridges in the South Atlantic as a significant oceanic iron source, *Nature Geoscience*, *6*(9), 775-779, doi:10.1038/Ngeo1893.

Shchepetkin, A. F., and J. C. McWilliams (2005), The regional oceanic modeling system (ROMS): a split-explicit, free-surface, topography-following-coordinate oceanic model, *Ocean Modelling*, *9*(4), 347-404, doi:10.1016/j.ocemod.2004.08.002.

Somes, C. J., A. W. Dale, K. Wallmann, F. Scholz, W. Yao, A. Oschlies, J. Muglia, A. Schmittner, and E. P. Achterberg (2021), Constraining Global Marine Iron Sources and Ligand-Mediated Scavenging Fluxes With GEOTRACES Dissolved Iron Measurements in an Ocean Biogeochemical Model, *Global Biogeochemical Cycles*, *35*(8), doi:10.1029/2021gb006948.

Tagliabue, A., et al. (2010), Hydrothermal contribution to the oceanic dissolved iron inventory, *Nature Geoscience*, *3*(4), 252-256, doi:10.1038/ngeo818.

Tagliabue, A., A. R. Bowie, P. W. Boyd, K. N. Buck, K. S. Johnson, and M. A. Saito (2017), The integral role of iron in ocean biogeochemistry, *Nature*, *543*(7643), 51-59, doi:10.1038/nature21058.

Tagliabue, A., A. R. Bowie, T. Holmes, P. Latour, P. van der Merwe, M. Gault-Ringold, K. Wuttig, and J. A. Resing (2022), Constraining the Contribution of Hydrothermal Iron to Southern Ocean Export Production Using Deep Ocean Iron Observations, *Frontiers in Marine Science*, *9*, doi:10.3389/fmars.2022.754517.

Tagliabue, A., and J. Resing (2016), Impact of hydrothermalism on the ocean iron cycle, *Philosophical transactions. Series A, Mathematical, physical, and engineering sciences*, *374*(2081), doi:10.1098/rsta.2015.0291.

Tanaka, T., I. Yasuda, K. Kuma, and J. Nishioka (2012), Vertical turbulent iron flux sustains the Green Belt along the shelf break in the southeastern Bering Sea, *Geophysical Research Letters*, *39*(8), n/a-n/a, doi:10.1029/2012gl051164.

Thurnherr, A. M., K. J. Richards, C. R. German, G. F. Lane-Serff, and K. G. Speer (2002), Flow and Mixing in the Rift Valley of the Mid-Atlantic Ridge, *Journal of Physical Oceanography*, *32*(6), 1763-1778, doi:10.1175/1520-0485(2002)032<1763:Famitr>2.0.Co;2.

Vic, C., J. Gula, G. Roullet, and F. Pradillon (2018), Dispersion of deep-sea hydrothermal vent effluents and larvae by submesoscale and tidal currents, *Deep Sea Research Part I: Oceanographic Research Papers*, *133*, 1-18, doi:10.1016/j.dsr.2018.01.001.

This article is protected by copyright. All rights reserved.

Accepted Article

19448007, ja, Downloaded from https://agupubs.onlinelibrary.wiley.com/doi/10.1029/2022GL100615 by University of California - Los Ange, Wiley Online Library on [09/11/2022]. See the Terms and Conditions (https://onlinelibrary.wiley.com/terms-and-conditions) on Wiley Online Library for rules of use; OA articles are governed by the applicable Creative Commons License

Vic, C., A. C. Naveira Garabato, J. A. M. Green, A. F. Waterhouse, Z. Zhao, A. Melet, C. de Lavergne, M. C. Buijsman, and G. R. Stephenson (2019), Deep-ocean mixing driven by small-scale internal tides, *Nature communications*, *10*(1), 2099, doi:10.1038/s41467-019-10149-5.

Wong, K. H., J. Nishioka, T. Kim, and H. Obata (2022), Long-Range Lateral Transport of Dissolved Manganese and Iron in the Subarctic Pacific, *Journal of Geophysical Research: Oceans*, *127*(2), doi:10.1029/2021jc017652.

Yagi, M., and I. Yasuda (2012), Deep intense vertical mixing in the Bussol' Strait, *Geophysical Research Letters*, *39*(1), n/a-n/a, doi:10.1029/2011gl050349.

Yearsley, J. M., D. M. Salmanidou, J. Carlsson, D. Burns, and C. L. Van Dover (2020), Biophysical models of persistent connectivity and barriers on the northern Mid-Atlantic Ridge, *Deep Sea Research Part II: Topical Studies in Oceanography*, *180*, doi:10.1016/j.dsr2.2020.104819.

This article is protected by copyright. All rights reserved.

Accepted Article

19448007, ja, Downloaded from https://agupubs.onlinelibrary.wiley.com/doi/10.1029/2022GL100615 by University of California - Los Ange, Wiley Online Library on [09/11/2022]. See the Terms and Conditions (https://onlinelibrary.wiley.com/terms-and-conditions) on Wiley Online Library for rules of use; OA articles are governed by the applicable Creative Commons License

Accepted Article

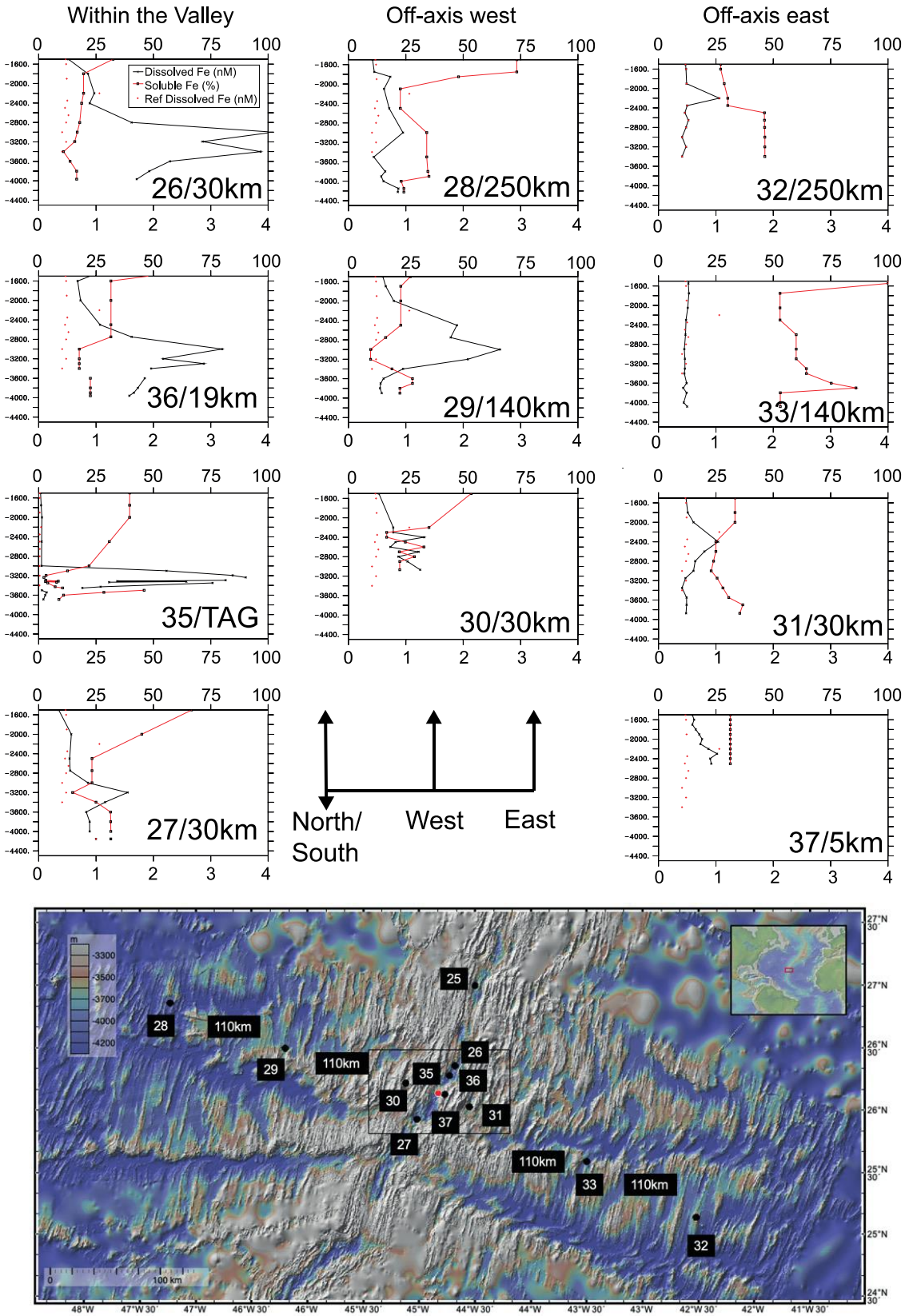


Figure 1. Vertical profiles of dissolved Fe (nM, black line, bottom x-axis), percentage of dFe present as soluble Fe (%, red line, top x-axis) and the iron profile from a reference station (station 32, red dots, nM) for the rage of stations within and outside

This article is protected by copyright. All rights reserved.

19448007, ja, Downloaded from https://agupubs.onlinelibrary.wiley.com/doi/10.1029/2022GL100615 by University of California - Los Ange, Wiley Online Library on [09/11/2022]. See the Terms and Conditions (https://onlinelibrary.wiley.com/terms-and-conditions) on Wiley Online Library for rules of use; OA articles are governed by the applicable Creative Commons License

the axial valley. The left-hand column shows stations within the valley, the central column shows stations from the west and the rightmost column shows stations to the east. Consult the map and supplementary figure 1 for more information on the stations and their spacing. Distances noted on each panel are the km from TAG, which is indicated by a red circle.

Accepted Article

This article is protected by copyright. All rights reserved.

19448007, ja, Downloaded from https://agupubs.onlinelibrary.wiley.com/doi/10.1029/2022GL100615 by University of California - Los Ange, Wiley Online Library on [09/11/2022]. See the Terms and Conditions (https://onlinelibrary.wiley.com/terms-and-conditions) on Wiley Online Library for rules of use; OA articles are governed by the applicable Creative Commons License

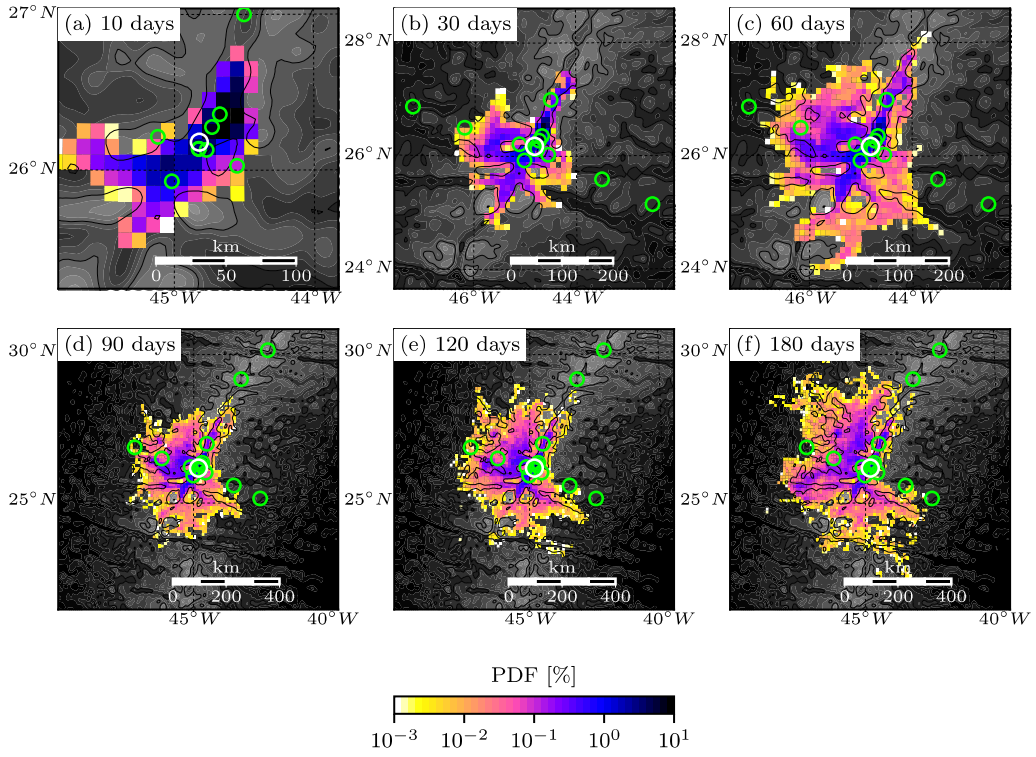


Figure 2. Probability density function of particle presence after (a) 10, (b) 30, (c) 60, (d) 90, (e) 120 and (f) 180 days of dispersion from TAG (white circle). Individual positions are binned onto a 0.1-degree resolution grid. Green circles are the Fridge stations.

Accepted Article

This article is protected by copyright. All rights reserved.

19448007, ja, Downloaded from https://agupubs.onlinelibrary.wiley.com/doi/10.1029/2022GL100615 by University of California - Los Ange, Wiley Online Library on [09/11/2022]. See the Terms and Conditions (https://onlinelibrary.wiley.com/terms-and-conditions) on Wiley Online Library for rules of use; OA articles are governed by the applicable Creative Commons License

Accepted Article

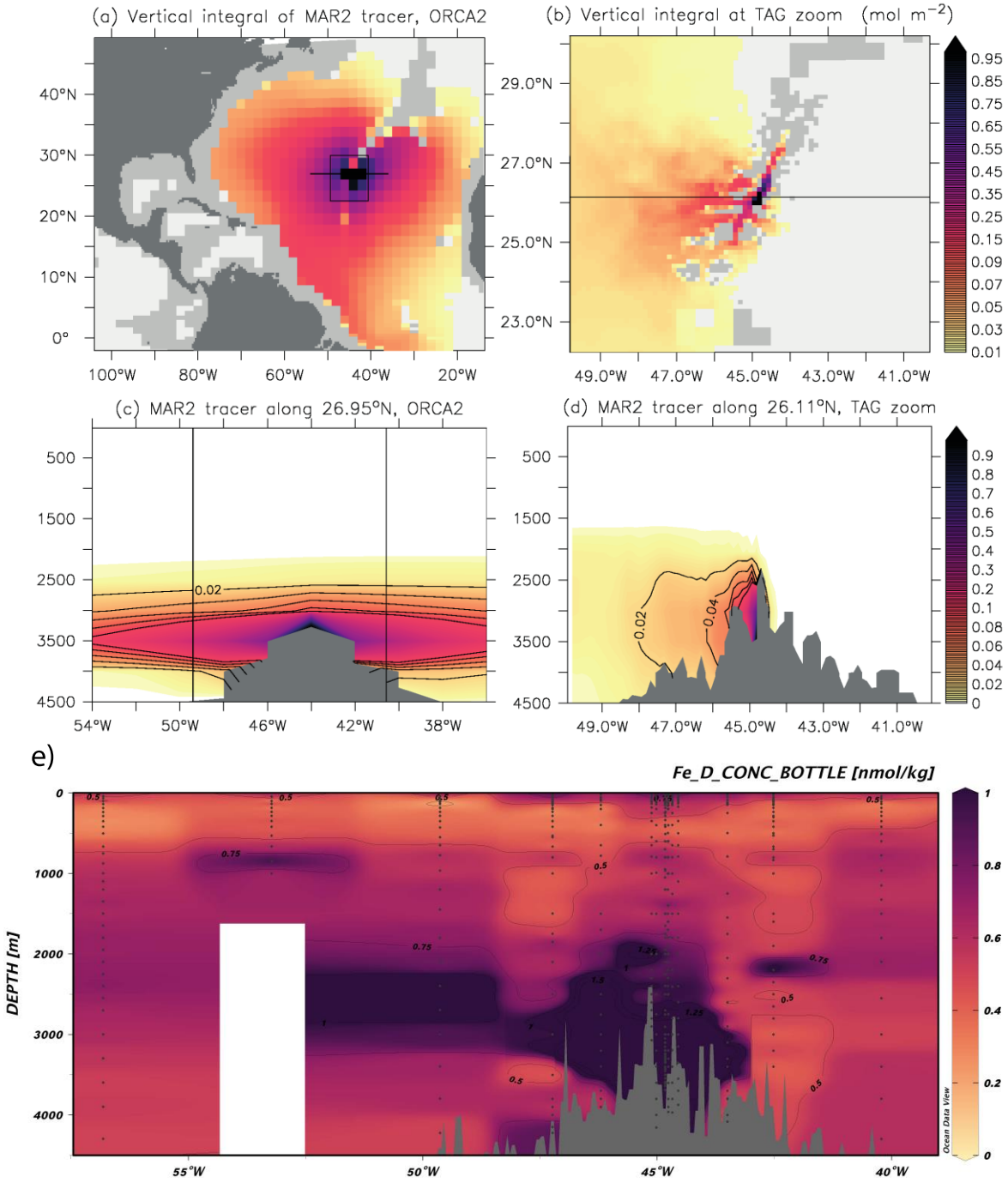


Figure 3. Vertically integrated tracer concentrations from an idealised tracer released from TAG in two model configurations: (a) the coarse global ORCA2 configuration and (b) a nested high-resolution AGRIF configuration. Panels (c) and (d) represent the tracer concentrations along a zonal section for the ORCA and AGRIF configurations, respectively. Panel (e) displays the merged GEOTRACES DFe concentration data (nmol/kg) from the GA03 and GA13 voyages that crossed the same region.

This article is protected by copyright. All rights reserved.

19448007, ja, Downloaded from https://agupubs.onlinelibrary.wiley.com/doi/10.1029/2022GL100615 by University of California - Los Ange, Wiley Online Library on [09/11/2022]. See the Terms and Conditions (https://onlinelibrary.wiley.com/terms-and-conditions) on Wiley Online Library for rules of use; OA articles are governed by the applicable Creative Commons License

Accepted Article

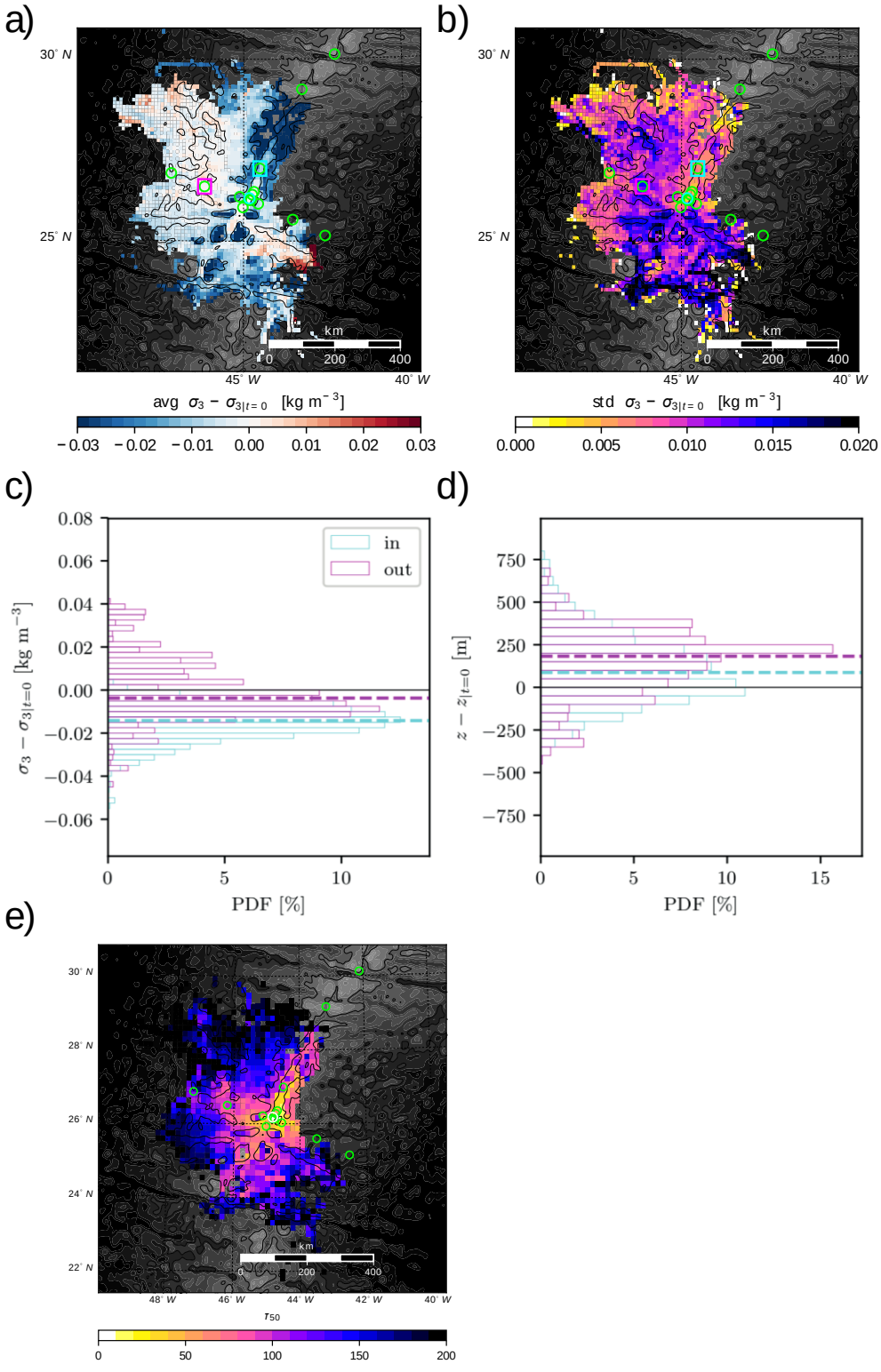


Figure 4. a) mean and b) standard deviation of the cumulative density change relative to initial density. Panels c) and d) represent histograms of density and absolute depth for particles inside and outside the valley (see squares on map on

This article is protected by copyright. All rights reserved.

19448007, ja, Downloaded from https://agupubs.onlinelibrary.wiley.com/doi/10.1029/2022GL100615 by University of California - Los Ange, Wiley Online Library on [09/11/2022]. See the Terms and Conditions (https://onlinelibrary.wiley.com/terms-and-conditions) on Wiley Online Library for rules of use; OA articles are governed by the applicable Creative Commons License

panel a). e) Median ages (in days) of particles at the depth of maximum particle density after 6 months of model simulation

Accepted Article

This article is protected by copyright. All rights reserved.

19448007, ja, Downloaded from https://agupubs.onlinelibrary.wiley.com/doi/10.1029/2022GL100615 by University of California - Los Ange, Wiley Online Library on [09/11/2022]. See the Terms and Conditions (https://onlinelibrary.wiley.com/terms-and-conditions) on Wiley Online Library for rules of use; OA articles are governed by the applicable Creative Commons License